Electric-Field-Driven Reversible Conversion Between Methylammonium Lead Triiodide Perovskites and Lead Iodide at Elevated Temperatures

*Yongbo Yuan, Qi Wang, Yuchuan Shao, Haidong Lu, Tao Li, Alexei Gruverman, and Jinsong Huang**

Solution-processed solar cells based on organolead trihalide perovskite (OTP) materials are emerging as a new generation of photovoltaic devices due to their low cost and superior performance.[1–17] The power conversion efficiency (PCE) of the perovskite solar cells increased dramatically from 3.8% to over 20% after only a few years of research.[1–7,9–16,18–22] The advances in low-cost, high-throughput processing methods, such as doctor-blading and spray coating, are also fast, which allowed fabrication of high-efficiency large-scale devices.[23–28] One of the remaining issues is whether the OTP materials and devices have sufficient stability that is needed for the commercialization of the OTP solar cells.[3,29,30] Among all factors that cause the instability of the hybrid perovskites, ion migration has been recently been identified to be intrinsic to the hybrid perovskite polycrystalline films and cannot be removed by device encapsulation. To solve the instability problem of the OTP-based devices, a deeper insight into the ion migration effect is necessary, since it might provide hints for the development of new materials with better stability.[30,31]

A first step in understanding the ion migration in methylammonium lead triiodide ($MAPbI_3$) is to identify the migrating species in the solar-cell grade polycrystalline thin films. Our first report of the giant switchable photovoltaic effect in OTP solar cells suggested that the mobile ions were positively charged methylammonium ions (MA^+) or/and iodine vacancies ($V_I^{\bullet}$).[32] Our subsequent measurements by means of photothermal-induced resonance (PTIR), which has a selective sensitivity to MA^+ species only, confirmed that the MA^+ ions in $MAPbI_3$ could migrate over tens of micrometers under a weak electrical field of 0.3 V μm^{-1}.[33] This indicates that the MA^+ ions migrate under the built-in electrical field of the operating solar cells.[8] It was later found that this effect actually enhances the device performance due to the improved p-i-n structure, in contrast to the general belief that ion migration would impair device efficiency.[34] On the other hand, migration of the iodine vacancies ($V_I^{\bullet}$) has not been yet experimentally observed. Theoretical calculations suggest that the $V_I^{\bullet}$ might be even more mobile than MA^+ ions, although the activation energy values for $V_I^{\bullet}$ migration calculated by different methods vary from 0.08 to 0.58 eV.[35,36] In view of the widely observed oxygen vacancies migration in many oxide perovskite materials, the assumption of $V_I^{\bullet}$ migration in $MAPbI_3$ materials is quite reasonable.

In this contribution, we present a direct evidence for the macroscopic migration of $V_I^{\bullet}$ in $MAPbI_3$ perovskite films at an elevated temperature of 330 K. Most interestingly, we report a reversible conversion between $MAPbI_3$ and lead iodide (PbI_2) phases under a small electric field at the elevated temperature as a result of a set of solid-state chemical reactions, and show that the conversion of $MAPbI_3$ to PbI_2 is slower than the conversion of PbI_2 to $MAPbI_3$ at room temperature (RT).

The $MAPbI_3$ lateral devices were fabricated on glass substrates to enable observation of ion migration process by an optical microscope or a charge-coupled device (CCD) camera. **Figure 1**a shows the working area of a fresh $MAPbI_3$ device at 330 K in vacuum taken with the CCD camera. The cross-sectional structure of the device is illustrated in Figure 1b. After applying a constant electrical field of ≈3 V μm^{-1} for 20–60 s, a thread formed near the anode region, and then gradually moved toward the cathode along the applied electric field direction. Figure 1c,e show the snapshot optical images obtained during the migration of this thread under the applied electric field. Sketches in Figure 1b,d,f illustrate a change in the device cross-section due to the formation of the thread (red region) and its subsequent motion across the channel from the anode to the cathode. (The process of thread formation and its motion can be seen in Video S1, Supporting Information). The thread appears darker than the neighboring regions due to the scattering of light incident at an angle of 50°–60°. When observed with vertical incident light in reflection mode, the thread (region B) has a similar color with the neighboring regions (Figure 1g). The optical microscopy image in transmission mode in Figure 1h shows that this thread has higher transparency than the neighboring regions.

To determine composition of the formed thread, we conducted energy-dispersive X-ray spectroscopy (EDX) and X-ray diffraction analysis (XRD) measurements. The scanning electron microscope (SEM) (**Figure 2**a) and EDX images (Figure 2c–h) show the distributions of gold (Au), I and lead (Pb) elements in a device poled by an applied electric field of 3 V μm^{-1} for 1 min. The quantitative distribution of these elements along the

Dr. Y. Yuan, Dr. Q. Wang, Dr. Y. Shao, Prof. J. Huang
Department of Mechanical and Materials Engineering
University of Nebraska-Lincoln
Lincoln, NE 68588, USA
E-mail: jhuang2@unl.edu
Dr. H. Lu, Dr. T. Li, Prof. A. Gruverman
Department of Physics and Astronomy
University of Nebraska-Lincoln
Lincoln, NE 68588, USA

DOI: 10.1002/aenm.201501803

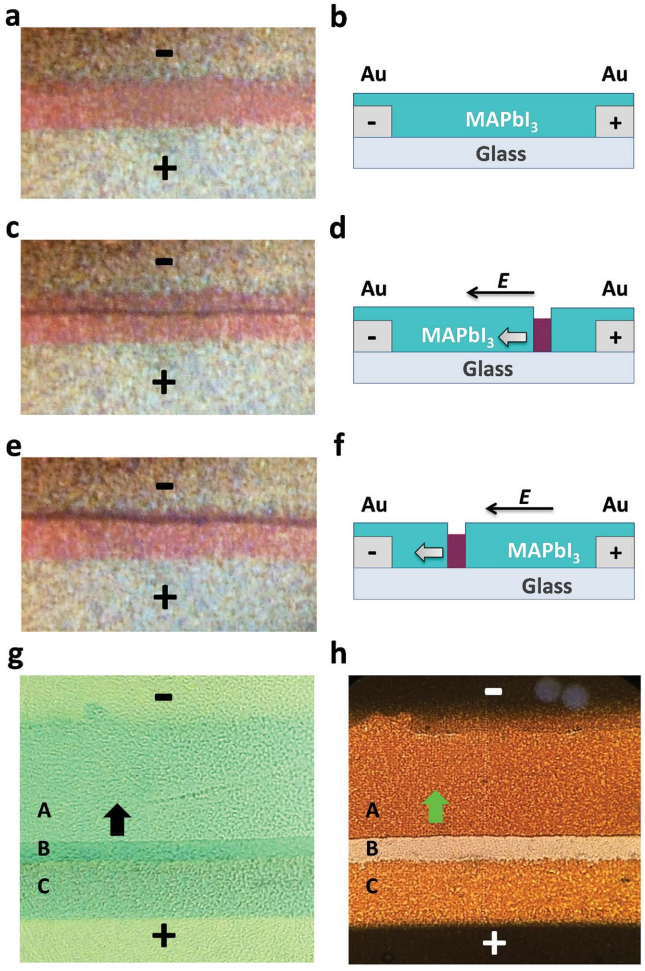

Figure 1. The formation of PbI_2 thread in $MAPbI_3$ by electrical poling at 330 K. Optical images of the lateral $MAPbI_3$ perovskite solar cells: a) without PbI_2 thread, and c,e) with a PbI_2 thread at different locations; Cross-sectional illustrations of b) the lateral $MAPbI_3$ perovskite devices without or d,f) with the PbI_2 thread; Comparison between the $MAPbI_3$ and the PbI_2 thread regions under optical microscope in g) the reflection mode and h) the optical transmission mode, where the arrows indicating the moving direction of the PbI_2 thread. The regions of A, B, and C are the fresh $MAPbI_3$, PbI_2 thread, and reformed $MAPbI_3$, respectively. The electrodes spacing is 100 μm.

dashed lines in Figure 2c,e,g are shown in Figure 2d,f,h, respectively. An I-deficiency is observed in the I-mapping image at the location of the thread in SEM (Figure 2e). The concentration of I^- anions in the thread region is about 50 ± 10 % of that in $MAPbI_3$ regions with a statistics acquired from six samples (Figure 2f and Figure S1, Supporting Information). Besides, a new XRD peak at ≈15° was observed after a thread formed in the lateral device after electrical poling, which is assigned to be the (001) diffraction peak of PbI_2 (Figure 2b). For a better XRD signal, large area lateral device with interdigitated electrodes was used for the XRD measurement (Figure S2, Supporting Information). As a consequence, we conclude the thread region is composed of PbI_2, which has a smaller I^- concentration than $MAPbI_3$. The migration of this I-deficient PbI_2 thread under the electric field conclusively proves the migration of I^- for the first time, because it must involve massive I^- anion transportation. Meanwhile, the distribution of Pb^{2+} cations after poling is found to be uniform in the thread and surrounding regions (Figure 2g,h), indicating that the migration of the Pb^{2+} cations is negligible. This result is consistent with previous theoretical calculations, which suggested that the activation energy for the Pb^{2+} cation migration of 2.3 eV is much larger than those of MA^+ and I^- ions (<1.0 eV).[35,36]

To summarize, the thread formed at 330 K moved toward cathode under the electrical field while maintaining its shape and width. This observation suggests that $MAPbI_3$ is converted into PbI_2 at the front edge of the thread (defined as the edge facing the cathode side), and reformed at the back edge of the thread (defined as the edge facing the anode side). Also, motion of the thread as an entire unit indicates that these two reversible conversion processes occur at the same rate so that the width of the thread is maintained while it moves. A higher transparency of the thread in comparison with the surrounding $MAPbI_3$ region can now be easily understood given that PbI_2 has a much larger bandgap and less absorption in visible range than $MAPbI_3$.[32,37]

For a better understanding of the formed PbI_2, the morphology and conductivity of the PbI_2 thread were studied by Kelvin probe force microscopy (KPFM) and conducting atomic force microscopy (c-AFM), with the results shown in **Figure 3**. Geometry of the KPFM measurements is illustrated in Figure 3a. A topographic image in Figure 3b shows an area of 50 μm × 50 μm with the 5 μm wide PbI_2 thread. Typically, the width of PbI_2 thread is 10 μm ± 5 μm, which varies from sample to sample and is determined by the formation stage. The height profile along the dashed line in Figure 3b is shown in Figure 3c. The total thickness of the $MAPbI_3$ film was ≈280 nm, and the thread was ≈70 nm thinner than the $MAPbI_3$ film. Despite of its reduced thickness, the amount of Pb ions in the thread is unchanged (Figure 2h). Therefore, the reduced thread thickness can be caused only by the loss of MA^+ and I^- ions. Figure 3c also shows that both the front and back edges between the $MAPbI_3$ and PbI_2 are quite sharp. The reformed $MAPbI_3$ (Region A) has nearly the same height of about 280 nm with fresh $MAPbI_3$ (Region C), which means the conversion of PbI_2 back to $MAPbI_3$ is complete, and there is a relatively small loss of MA^+ and I^- ions in the form of vapor. It agrees with the observed comparable amount of I^- in the regions before (Region A) and after (Region C) the thread swept over, as shown in Figure 2f. The adhesive (Figure 3d) and phase (see Figure S3, Supporting Information) mapping shows that the PbI_2 thread is less adhesive and more rigid than that of the surrounding $MAPbI_3$.

Conductivity of the PbI_2 thread along two typical directions, i.e., across (Figure 3a) and along (Figure 3g) the thread, has been investigated by KPFM and c-AFM, respectively. In the KPFM measurement, by applying a constant bias between the two electrodes, there is a uniform current flowing throughout the measured region, while the surface potential drops gradually from anode to cathode (Figure 3f). The conductivity of the materials at different locations can be estimated from the slope of the potential-position curve. Figure 3e shows that the potential drop across the PbI_2 thread is ≈50–100 times faster than that across the fresh $MAPbI_3$ film. Therefore, almost all the potential applied to the device drops at the PbI_2 thread

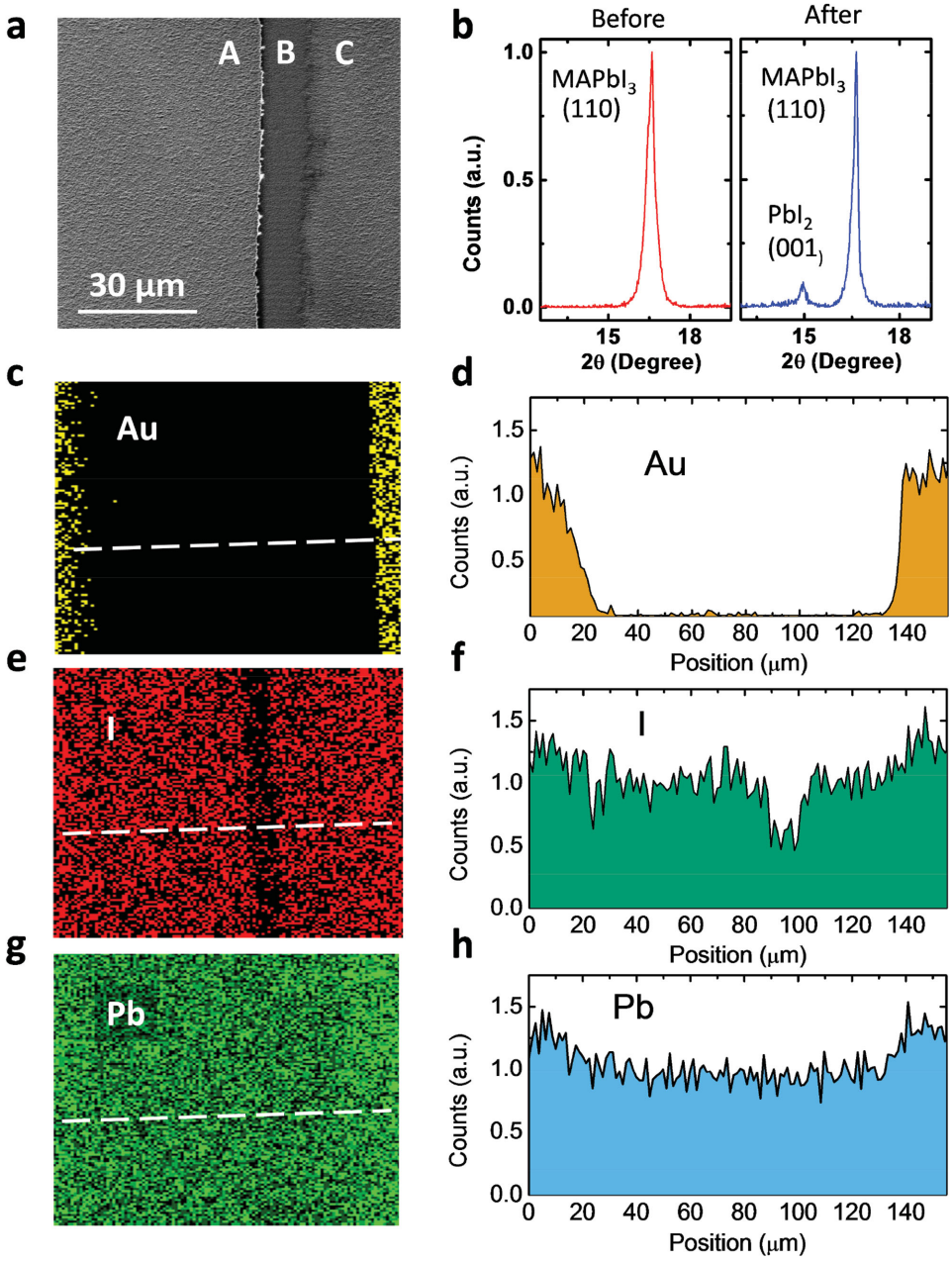

Figure 2. EDX and XRD study of the lateral devices with a PbI_2 thread. a) SEM image of a typical PbI_2 thread, where an area of 80 µm × 85 µm was shown (electrode area was not included for a better clarity). b) XRD spectra of the $MAPbI_3$ film before and after the formation of a PbI_2 thread. For a better signal/noise ratio, a large area lateral device with interdigitated electrode (see Figure S2, Supporting Information) was used for the electrical poling and XRD measurement. Concentration mapping of c) gold, e) iodine, and g) lead elements in a lateral device with a PbI_2 thread, where the electrode spacing is 100 µm and the measured area is 150 µm × 120 µm. Concentration profiles of d) gold, f) iodine, and h) lead in the location that marked in (c). The position of two electrodes can be well recognized from the Au atoms distributions shown in Figure 2c.

(Figure 3f). In the c-AFM measurements, an additional Au electrode bar was deposited perpendicular to the PbI_2 thread as ground electrode, as illustrated in Figure 3g. By placing the c-AFM tip inside or outside the PbI_2 thread, the conductivity of the formed PbI_2 and $MAPbI_3$ (both fresh and reformed) can be measured by applying a bias between the tip and the Au electrode. In Figure 3h, lateral currents obtained in fresh $MAPbI_3$ (Region A), and reformed $MAPbI_3$ (Region C) are I_A (6 pA) and I_C (2 pA), respectively, which are 60 and 20 times higher than the lateral current obtained in PbI_2 ($I_B < 0.1$ pA, limited by the equipment resolution), respectively. Both the KPFM and c-AFM results indicate that it is highly unlikely that the PbI_2 thread is heavily doped. The reformed $MAPbI_3$ is also found to be less conductive than the fresh $MAPbI_3$, which might be due to the formation of a large density of defects, e.g., grain boundaries, or spatial variations in composition, or changed doping.[38]

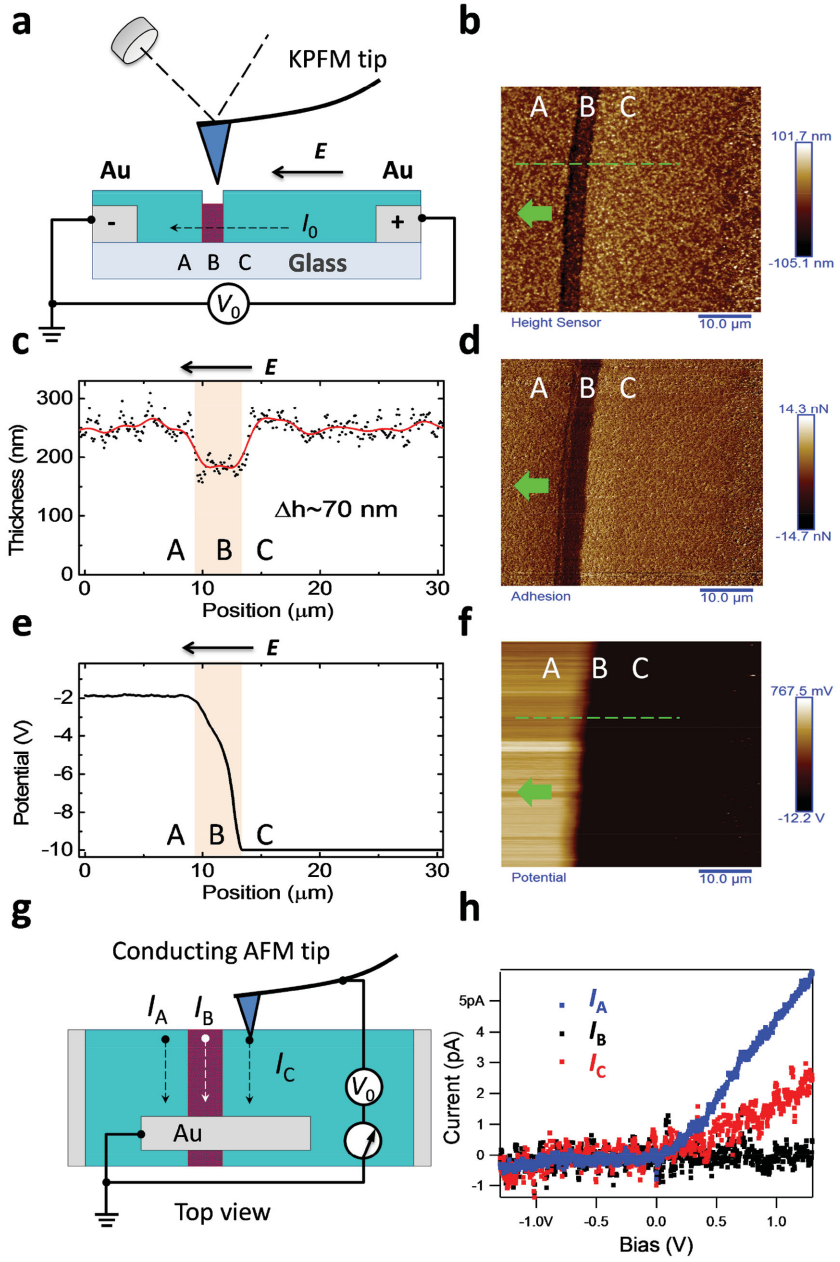

Figure 3. Electronic properties of the $MAPbI_3$ and PbI_2 regions. a) Schematic illustration of the KPFM measurement around the PbI_2 thread, where a constant bias of 10 V was applied on the anode electrode (the arrow indicates the direction of the electric field and current flow); b) topography image, d) adhesive image, and f) surface potential mapping of the $MAPbI_3$ film with fresh $MAPbI_3$ (Region A), PbI_2 (Region B) and reformed $MAPbI_3$ (Region C), respectively, where the arrows show the direction of the PbI_2 thread migration. c) Height profile of the $MAPbI_3$ film for the position marked in Figure 3 b; e) Surface potential profile around the PbI_2 thread for the position marked in Figure 3f; g) Schematic illustration of the c-AFM measurement around the PbI_2 domain, where an additional Au electrode bar was deposited on the top as the ground electrode, and electric current flows in parallel to the PbI_2 thread. h) Local current–voltage curve measured with the c-AFM tip in contacting with fresh $MAPbI_3$ (Region A), PbI_2 domain (Region B) and reformed $MAPbI_3$ (Region C), respectively.

After confirming that the material in the thread is PbI_2, it is of great importance to understand how the PbI_2 thread is generated and why it could migrate inside the $MAPbI_3$ film under the electric field. We propose that these phenomena are caused by a set of electrochemical reactions at the electrodes and solid-state reactions mediated by the massive migration of I^- and MA^+ ions, as illustrated in **Figure 4**. The experimental results pointed out that the PbI_2 thread was generated around the Au anode, which can be explained by the following solid-state and electrochemical reactions:

$$MAPbI_3 \rightarrow PbI_2 + MA^+ + I^- \quad (1)$$

$$2I^- \rightarrow I_2 \uparrow + 2e^- \quad (2)$$

Due to the low thermal stability of $MAPbI_3$, it can decompose to the two precursors of MAI and PbI_2, which is facilitated by the temperature increase to 330 K. The I^- anions are electrochemically reduced to I_2 vapor by the Au anode, causing a loss of I^- under the gold anode region. In some of our experiments based on $MAPbI_3$ single crystal, we could observe a quick release of colored I_2 vapor from the anode region under application of an electrical field of 0.2 V μm^{-1}, which confirmed the proposed scenario. The residual MA^+ ions are quickly driven away from the anode toward the cathode region by the applied electric field, which was verified by our previous PTIR studies of MA^+ migration at room temperature (RT).[33] The higher temperature used in the present experiments should further promote MA^+ migration. After cooling down from 330 to 300 K and removing the applied electric field, the formed PbI_2 phase is stable and persists even when exposed to ambient atmosphere. This fact is illustrated by images in Figure 1g,f and Figures 2 and 3, which were obtained after storing the samples in air for more than 10 hours.

Migration of the PbI_2 thread toward the Au cathode under the applied electric field indicates that the conversion of $MAPbI_3$ to the PbI_2 at the front edge of the PbI_2 thread can also occur without a direct contact of $MAPbI_3$ with the Au electrode. The only difference is that the I^- anions need to be removed away from the front edge by diffusion across the PbI_2 thread region. The fact that PbI_2 thread maintained its width under a low electric field (Figure 1d) instead of spreading from anode to cathode by the migration of its front edge (Figure S4, Supporting Information) indicates that PbI_2 converted back to the $MAPbI_3$ phase at the back edge of the thread. This is a typical formation process of $MAPbI_3$ (Figure 4b):

$$I^- + PbI_2 + MA^+ \rightarrow MAPbI_3 \quad (3)$$

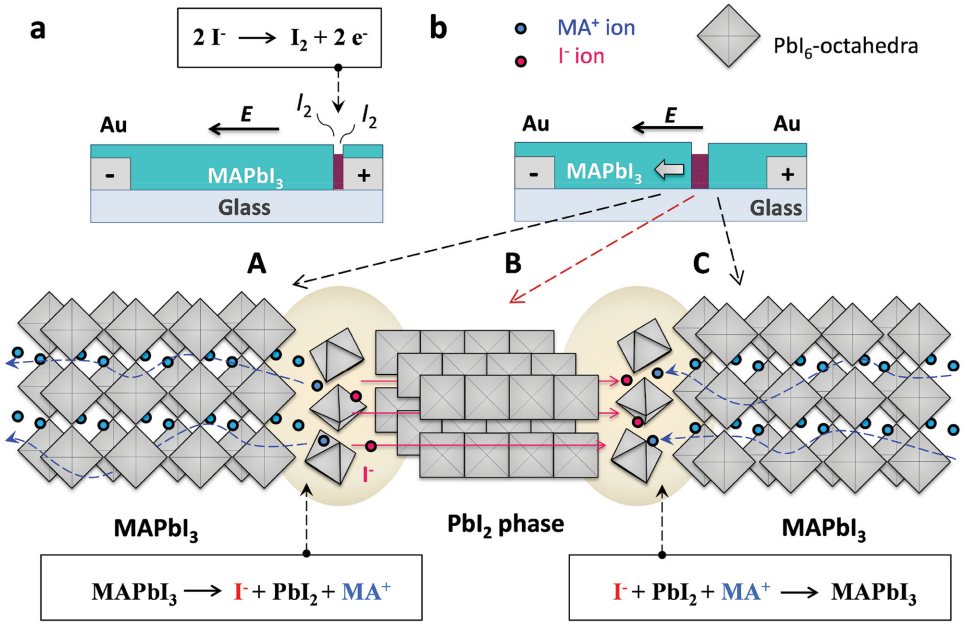

Figure 4. Reversible conversion between $MAPbI_3$ and PbI_2 under electric field. a) Cross-sectional illustrations of lateral $MAPbI_3$ perovskite solar cells with a PbI_2 thread forming below the anode. b) Illustrations of the lateral $MAPbI_3$ devices with the PbI_2 thread moving toward cathode, which is resulted from two sets of proposed solid-state chemical reactions occurring at the "Region A/Region B" and "Region B/Region C" interfaces, respectively.

where the I^- anions are generated by the decomposition of $MAPbI_3$ at the front edge (Region A) under the action of the applied field. This suggests that I^- ions must migrate across the PbI_2 thread, and some of the $MAPbI_3$ region as well, from the front to the back edge. The released MA^+ ions by Reaction (1) in region A do not take part in the Reaction (3) since it has an opposite migrating direction with that of I^- ions. The MA^+ cations are produced by the newly formed $MAPbI_3$ in region C. The migration of MA^+ ions is illustrated in Figure 4b (blue dash line). In some cases we observed that the PbI_2 thread had broadened at a higher electrical field (e.g., 3.5 V μm^{-1}, see Figure S5, Supporting Information), which can be explained by the difference in the limiting factors for the moving of the front edge and back edge of the thread. The decomposition of $MAPbI_3$ at the front edge of the thread is determined by the temperature and by how fast MA^+ and I^- can be removed away from the front edge, while the migration speed of the back edge of the PbI_2 thread is limited by the supplying amount of MA^+ and I^- at the back edge. A loss of I^- ions through I_2 vapor formation (Reaction (2)) under the large electric field, which removes iodine from the film, may cause insufficient supply of I^- at the back edge and cause the broadening of the PbI_2 thread.

Under a relatively low electric field (≈3 V μm^{-1}), the moving speed of the PbI_2 thread was found to increase with the applied electrical field (Figure S5, Supporting Information). When the applied electrical field increased from 2.5 to 3.5 V μm^{-1}, the time required for the thread to move across the 100 μm wide anode–cathode spacing decreased from ≈250 to ≈168 s. The corresponding ionic migration mobility is calculated to be $\approx 1.7 \times 10^{-9}$ cm^2 V^{-1} s^{-1} in both cases, which is very close to the ionic mobility of 1.5×10^{-9} cm^2 V^{-1} s^{-1} obtained in our previous study.[33] This observation suggests that the ionic migration mobility indeed determines the moving speed of the PbI_2 thread and conductivity of the $MAPbI_3$ perovskites at a relatively high temperature of 330 K.

Our experimental results indicate that conversion from $MAPbI_3$ to PbI_2 is more sensitive to temperature than the reverse process (Reaction (3)) under the same applied electric field, which can be explained by the exothermic nature of reaction (3). In our experiments, after forming the PbI_2 thread, we turned off the applied bias and decreased the temperature down to 300 K. When we tried to move the PbI_2 thread with the same electric field (3 V μm^{-1}) at 300 K, the PbI_2 thread disappeared (see the Video S2, Supporting Information). This observation indicates that the generated PbI_2 can still be efficiently converted to $MAPbI_3$ perovskite at RT, while the decomposition of $MAPbI_3$ to PbI_2 is slowed down at lower temperature. This also explains why the migration of the PbI_2 thread was not observed at RT in our previous studies.[32,33] Slower decomposition of $MAPbI_3$ to PbI_2 is actually good for the stability of solar cells at RT, while faster decomposition may limit operation of the perovskite solar cells at higher temperatures.

In summary, we have studied the migration of I^- ions in $MAPbI_3$ perovskite films at an elevated temperature of 330 K. For the first time, we present a direct visualization of macroscopic migration of a large amount of I^- ions in these films under an electric field. Electrically driven migration of the PbI_2 thread in $MAPbI_3$ film results from a set of solid-state chemical reactions that occur simultaneously at the front and back edges of the thread with comparable reaction rates. We also demonstrate that the conversion between the $MAPbI_3$ and PbI_2 phases induced by the electrical field is fully reversible at 330 K. The obtained results provide further insights into the ionic transport properties and electrochemical activities of the $MAPbI_3$ materials. Further studies are required to clarify the role of the surface and bulk diffusion mechanisms in the observed effect.

Experimental Section

Device Fabrication: The lateral $MAPbI_3$ device was fabricated on glass substrate. At first, 75 nm thick Au electrodes with spacing of 50 μm or 100 μm were thermally deposited by using shadow mask. Subsequently a 300 nm thick $MAPbI_3$ film was spin coated on substrate with a "two-step" interdiffusion method. In particular, PbI_2 (40 wt%) and MAI (4.0 wt%) were first dissolved in dimethylformamide and 2-propanol, respectively, to form precursor solutions. The PbI_2 hot solution was spun onto glass at 6000 rpm. Then the hot MAI solution was spin coated on PbI_2 film at 6000 Hz for 35 s. The bilayer films were then annealed at 100 °C for 1 h.

Film and Device Characterization: Measurements on lateral solar cells were conducted in a probe station chamber under a vacuum of 10^{-5} Pa, with white light (25 mW cm^{-2}) through a quartz window. The substrate was located on a metal plate with its temperature being controlled by a heater and injected liquid N_2, which can varied from 80 K to 340 K. A high voltage supply (Keithley 240a) with a maximum voltage output of 1200 V was used for the poling process. A semiconductor analyzer (Keithley 4200) was used for the current–voltage characterization.

Element Mapping by EDX: The EDX mapping was carried out on a FEI Nova NanoSEM 450 instrument equipped with an Oxford X-MAX energy-dispersive X-ray spectroscope. Typical electron acceleration voltage for X-ray excitation was 20 kV. The excited characteristic Mα X-ray from Pb (2.342 keV), Lα X-ray from I (3.937 keV) and Mα X-ray from Au (2.120 keV) was detected for element mapping, respectively.

XRD Measurement: XRD measurement were carried out with a Rigaku D/Max-B X-ray diffractometer with Bragg–Brentano parafocusing geometry, a diffracted beam monochromator, and a conventional cobalt target X-ray tube set to 40 KV and 30 mA. The emitted X-ray wavelength is 1.79 Å.

KPFM and AFM Measurements: Measurements were carried out in air and in the dark. Platinum-iridium-coated conductive probes were used in the KPFM and AFM measurements. The peak force KPFM mode, combining the tapping mode AFM with frequency modulation KPFM was used to measure the topographic and surface potential signals from the same sample area. The scanning area and tip velocity were 50 μm × 50 μm and 81.4 μm s^{-1}, respectively. The tip-surface distance for KPFM measurements was 80 nm for all samples. The conductivity of the $MAPbI_3$ film was measured by applying 10 V bias to devices with electrode spacing of 50 μm. The conductivity at different regions was extracted from the slope of the surface potential versus position curves.

C-AFM Measurement: Conducting AFM (MFP-3D, Asylum Research) was used to compare the conductivity of the $MPbI_3$ and PbI_2 films. The configuration of the testing is illustrated in Figure 3g, where the PbI_2 domain in the lateral $MAPbI_3$ device was first formed by electrical poling (2–4 V μm^{-1}) at 330 K, and then the sample was cooled down to room temperature and transferred to an evaporator for the deposition of Au electrode. After that the sample was electrically tested by c-AFM in air, with the Au electrode grounded.

The electrically poled $MAPbI_3$ film was observed under an optical microscope (Olympus BX61) coupled to a high-resolution CCD camera (Photometrics, CoolSNAP-cf). The optical microscope worked in the transmission (or reflection) mode with the sample illuminated from bottom (or top).

Supporting Information

Supporting Information is available from the Wiley Online Library or from the author.

Acknowledgements

Y.Y. and Q.W. contributed equally to this work. This research was supported by National Science Foundation Grant DMR-1505535, and through the Nebraska Materials Research Science and Engineering Center (MRSEC) under Grant DMR-1420645.

Received: September 11, 2015
Revised: November 4, 2015
Published online: December 2, 2015

[1] J. Burschka, N. Pellet, S.-J. Moon, R. Humphry-Baker, P. Gao, M. K. Nazeeruddin, M. Grätzel, *Nature* **2013**, *499*, 316.
[2] M. Liu, M. B. Johnston, H. J. Snaith, *Nature* **2013**, *501*, 395.
[3] A. Kojima, K. Teshima, Y. Shirai, T. Miyasaka, *J. Am. Chem. Soc.* **2009**, *131*, 6050.
[4] M. M. Lee, J. Teuscher, T. Miyasaka, T. N. Murakami, H. J. Snaith, *Science* **2012**, *338*, 643.
[5] A. Abrusci, S. D. Stranks, P. Docampo, H.-L. Yip, A. K. Y. Jen, H. J. Snaith, *Nano Lett.* **2013**, *13*, 3124.
[6] J. M. Ball, M. M. Lee, A. Hey, H. J. Snaith, *Energy Environ. Sci.* **2013**, *6*, 1739.
[7] G. Hodes, *Science* **2013**, *342*, 317.
[8] J. Y. Jeng, Y. F. Chiang, M. H. Lee, S. R. Peng, T. F. Guo, P. Chen, T. C. Wen, *Adv. Mater.* **2013**, *25*, 3727.
[9] H.-S. Kim, I. Mora-Sero, V. Gonzalez-Pedro, F. Fabregat-Santiago, E. J. Juarez-Perez, N.-G. Park, J. Bisquert, *Nat. Commun.* **2013**, *4*, 2242.
[10] N.-G. Park, *J. Phys. Chem. Lett.* **2013**, *4*, 2423.
[11] H. J. Snaith, *J. Phys. Chem. Lett.* **2013**, *4*, 3623.
[12] S. D. Stranks, G. E. Eperon, G. Grancini, C. Menelaou, M. J. Alcocer, T. Leijtens, L. M. Herz, A. Petrozza, H. J. Snaith, *Science* **2013**, *342*, 341.
[13] W. Zhang, M. Saliba, S. D. Stranks, Y. Sun, X. Shi, U. Wiesner, H. J. Snaith, *Nano Lett.* **2013**, *13*, 4505.
[14] G. Xing, N. Mathews, S. Sun, S. S. Lim, Y. M. Lam, M. Grätzel, S. Mhaisalkar, T. C. Sum, *Science* **2013**, *342*, 344.
[15] J. H. Heo, S. H. Im, J. H. Noh, T. N. Mandal, C.-S. Lim, J. A. Chang, Y. H. Lee, H.-J. Kim, A. Sarkar, M. K. Nazeeruddin, *Nat. Photonics* **2013**, *7*, 486.
[16] P. Docampo, J. M. Ball, M. Darwich, G. E. Eperon, H. J. Snaith, *Nat. Commun.* **2013**, *4*, 2761.
[17] H.-S. Kim, C.-R. Lee, J.-H. Im, K.-B. Lee, T. Moehl, A. Marchioro, S.-J. Moon, R. Humphry-Baker, J.-H. Yum, J. E. Moser, *Sci. Rep.* **2012**, *2*, 591.
[18] J. Y. Jeng, Y. F. Chiang, M. H. Lee, S. R. Peng, T. F. Guo, P. Chen, T. C. Wen, *Adv. Mater.* **2013**, *25*, 3727.
[19] N.-G. Park, *J. Phys. Chem. Lett.* **2013**, *4*, 2423.
[20] J.-H. Im, C.-R. Lee, J.-W. Lee, S.-W. Park, N.-G. Park, *Nanoscale* **2011**, *3*, 4088.
[21] W. S. Yang, J. H. Noh, N. J. Jeon, Y. C. Kim, S. Ryu, J. Seo, S. I. Seok, *Science* **2015**, *12*, 9272.
[22] N. Ahn, D.-Y. Son, I.-H. Jang, S. M. Kang, M. Choi, N.-G. Park, *J. Am. Chem. Soc.* **2015**, *137*, 8696.
[23] Y. Deng, E. Peng, Y. Shao, Z. Xiao, Q. Dong, J. Huang, *Energy Environ. Sci.* **2015**, *8*, 1544.
[24] K. Hwang, Y. S. Jung, Y. J. Heo, F. H. Scholes, S. E. Watkins, J. Subbiah, D. J. Jones, D. Y. Kim, D. Vak, *Adv. Mater.* **2015**, *27*, 1241.
[25] H. S. Kim, S. K. Kim, B. J. Kim, K.-S. Shin, M. G. Kumar, H. S. Jung, S.-W. Kim, N.-G. Park, *J. Phys. Chem. Lett.* **2015**, *6*, 1729.
[26] Z. Yang, C.-C. Chueh, F. Zuo, J. H. Kim, P.-W. Liang, A. K. Y. Jen, *Adv. Energy Mater.* **2015**, *5*, 1500328.
[27] A. T. Barrows, A. J. Pearson, C. K. Kwak, A. D. Dunbar, A. R. Buckley, D. G. Lidzey, *Energy Environ. Sci.* **2014**, *7*, 2944.
[28] D. Sanjib, B. Yang, G. Gu, P. C. Joshi, I. N. Ivanov, C. M. Rouleau, T. Aytug, D. B. Geohegan, K. Xiao, *ACS Photonics* **2015**, *2*, 680.

[29] T.-B. Song, Q. Chen, H. Zhou, C. Jiang, H.-H. Wang, Y. M. Yang, Y. Liu, J. You, Y. Yang, *J. Mater. Chem. A* **2015**, *3*, 9032.
[30] I. C. Smith, E. T. Hoke, D. Solis-Ibarra, M. D. McGehee, H. I. Karunadasa, *Angew. Chem. Int. Ed.* **2014**, *126*, 11414.
[31] J. H. Noh, S. H. Im, J. H. Heo, T. N. Mandal, S. I. Seok, *Nano Lett.* **2013**, *13*, 1764.
[32] Z. Xiao, Y. Yuan, Y. Shao, Q. Wang, Q. Dong, C. Bi, P. Sharma, A. Gruverman, J. Huang, *Nat. Mater.* **2015**, *14*, 193.
[33] Y. Yuan, J. Chae, Y. Shao, Q. Wang, Z. Xiao, A. Centrone, J. Huang, *Adv. Energy Mater.* **2015**, *5*, 1500615.
[34] Y. Deng, Z. Xiao, J. Huang, *Adv. Energy Mater.* **2015**, *5*, 1500721.
[35] J. M. Azpiroz, E. Mosconi, J. Bisquert, F. De Angelis, *Energy Environ. Sci.* **2015**, *8*, 2118.
[36] C. Eames, J. M. Frost, P. R. Barnes, B. C. O'regan, A. Walsh, M. S. Islam, *Nat. Commun.* **2015**, *6*, 7497.
[37] Q. Chen, H. Zhou, T.-B. Song, S. Luo, Z. Hong, H.-S. Duan, L. Dou, Y. Liu, Y. Yang, *Nano Lett.* **2014**, *14*, 4158.
[38] Q. Wang, Y. Shao, H. Xie, L. Lyu, X. Liu, Y. Gao, J. Huang, *Appl. Phys. Lett.* **2014**, *105*, 163508.

